Kim, Y. H. & Hossain, M. S. (2015). *Géotechnique* **65**, No. 12, 1029–1037 [http://dx.doi.org/10.1680/geot.15.T.008]

TECHNICAL NOTE

Dynamic installation of OMNI-Max anchors in clay: numerical analysis

Y. H. KIM* and M. S. HOSSAIN*

This paper reports the results from three-dimensional dynamic finite-element analysis undertaken to provide insight into the behaviour of OMNI-Max™ anchors during dynamic installation in non-homogeneous clay. The large-deformation finite-element analyses were carried out using the coupled Eulerian–Lagrangian approach, modifying the simple elastic–perfectly plastic Tresca soil model to allow strain softening, and incorporate strain-rate dependency of the shear strength using the Herschel–Bulkley model. The results were validated against field data prior to undertaking a detailed parametric study, exploring the relevant range of parameters in terms of anchor mass, impact velocity and soil strength. To predict the embedment depth in the field, an improved rational analytical embedment model, based on the total energy method, was proposed, with the large-deformation finite-element data used to calibrate the model.

KEYWORDS: anchors; clays; numerical modelling; offshore engineering

INTRODUCTION

Dynamically installed anchors (DIAs) are the most recent generation of anchoring systems for mooring floating facilities for deep water oil and gas developments. During installation, the anchor is released from a specified height above the seabed. This allows the anchor to gain velocity as it falls freely through the water column before impacting the seafloor and embedding into the sediments.

In recent years, broadly two DIA geometries have evolved. Torpedo anchors are rocket-shaped, typically consist of a long shaft, with the loading point (or padeye) attached at the top, and may feature up to four relatively small fins at the trailing edge (Brandão *et al*., 2006; Lieng *et al*., 2010). OMNI-Max™ anchors feature three large fins with intermittent discontinuity to accommodate an arm that transfers the loading point nearer to the head of the anchor (Zimmerman *et al*., 2009; Nie & Shelton, 2011; Shelton *et al*., 2011).

For dynamic installation of torpedo anchors in clay, a number of investigations have been carried out (e.g. O'Loughlin *et al*., 2004; Richardson *et al*., 2009; Nazem *et al*., 2012; Chow *et al*., 2014; Hossain *et al*., 2014, 2015). Investigations on OMNI-Max anchors are sparse. In this study, a numerical framework was developed for undertaking three-dimensional (3D) dynamic large-deformation finite-element (LDFE) analysis accounting for frictional resistance along the surfaces of the anchor, strain rate dependency and gradient of the soil undrained shear strength. Analyses on the complicated geometry of OMNI-Max anchors were carried out for the first time, and the results are reported here. The results from analyses on torpedo anchors have been reported by Kim *et al*. (2015).

REPORTED DATA FROM FIELD INSTALLATION

Zimmerman *et al*. (2009) and Shelton *et al*. (2011) noted that 160 OMNI-Max anchors were installed for temporary moorings in the Gulf of Mexico. The data from eight installations were reported in detail. The anchors with identical geometric dimensions (given in Table 1 referring to anchor A1, see also Fig. 1) and dry weight $W_d = 390$ kN (submerged weight $W_s = 341$ kN) were dropped from a drop height of $h_d = 50$ m. The soils were predominantly normally consolidated clay with undrained shear strength that increased with depth as $s_{u,ref} = 2{\cdot}4 + 1{\cdot}1z$ kPa. The achieved impact velocity was ~19 m/s and anchor tip embedment depths were $d_{e,t} = 10{\cdot}7$–$20{\cdot}1$ m.

In this study, parametric analyses were carried out mainly using geometry identical to anchor A1. Currently, the geometry of the anchor tip is slightly modified for better keying, and additional mass was considered to overcome higher strength of some clay sediments (Shelton *et al*., 2011; O'Loughlin *et al*., 2014). This is illustrated in Fig. 2(b), and dimensions are given in Table 1 (referred to as anchor A2). Additional analyses were also performed using this geometry.

For parametric study, the soil strengths considered included reported profiles at various locations in the Campos Basin, offshore Brazil; Vøring Plateau, Troll Field and Gjøa Field in the North Sea, off the western coast of Norway (Medeiros, 2002; de Araujo *et al*., 2004; Brandão *et al*., 2006; Zimmerman *et al*., 2009; Lieng *et al*., 2010), where torpedo anchors were installed.

NUMERICAL ANALYSIS

Analysis details

Three-dimensional LDFE analyses were carried out using the coupled Eulerian–Lagrangian (CEL) approach in the commercial finite-element package Abaqus/Explicit (Dassault Systèmes, 2011). To reduce the computational effort, the anchor dynamic installation was modelled from the soil surface, impacting the seabed with a velocity v_i.

Considering the symmetry of the problem, only one-half anchor and soil domain were modelled. The lateral extension and height of the soil domain were $26D_p$ from the centre of the anchor (D_p is the anchor frontal projected area (A_p) equivalent diameter) and $6{\cdot}5L_A$ respectively (as obtained from preliminary convergence studies; e.g. Kim *et al*. (2014))

Manuscript received 23 February 2015; revised manuscript accepted 6 July 2015. Published online ahead of print 2 September 2015. Discussion on this paper closes on 1 May 2016, for further details see p. ii.

* Centre for Offshore Foundation Systems (COFS), The University of Western Australia, Crawley, WA, USA.

Table 1. OMNI-Max anchor details

Description	Symbol	Anchor A1 (Zimmerman *et al.*, 2009)	Anchor A2 (O'Loughlin *et al.*, 2014)
Total anchor length	L_A	9·15 m	9·15 m
Head fin length	L_{HF}	2·47 m	2·47 m
Tail fin length	L_{TF}	5·12 m	5·12 m
Padeye length	L_{PE}	1·0 m	1·0 m
Fin thickness	t_F	0·1 m	0·1 m
Fin width	w_F	1·96 m	1·88 m
Padeye height	H_P	4·59 m	4·59 m
Padeye lever arm	w_P	2·18 m	2·18 m
Anchor shaft diameter	D_A	—	0·96 m
Anchor frontal projected area equivalent diameter	D_p	1·56 m	1·45 m
Anchor volume	V_A	5·02 m^3	8·96 m^3
Anchor dry weight	W_d	390 kN	697 kN
Anchor submerged weight	W_s	341 kN	609 kN

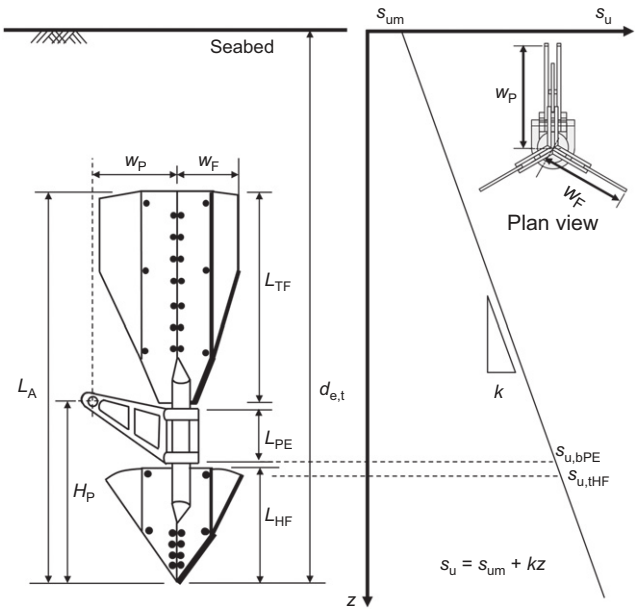

Fig. 1. Schematic diagram of installed OMNI-Max anchor in clay (anchor A1, Table 1)

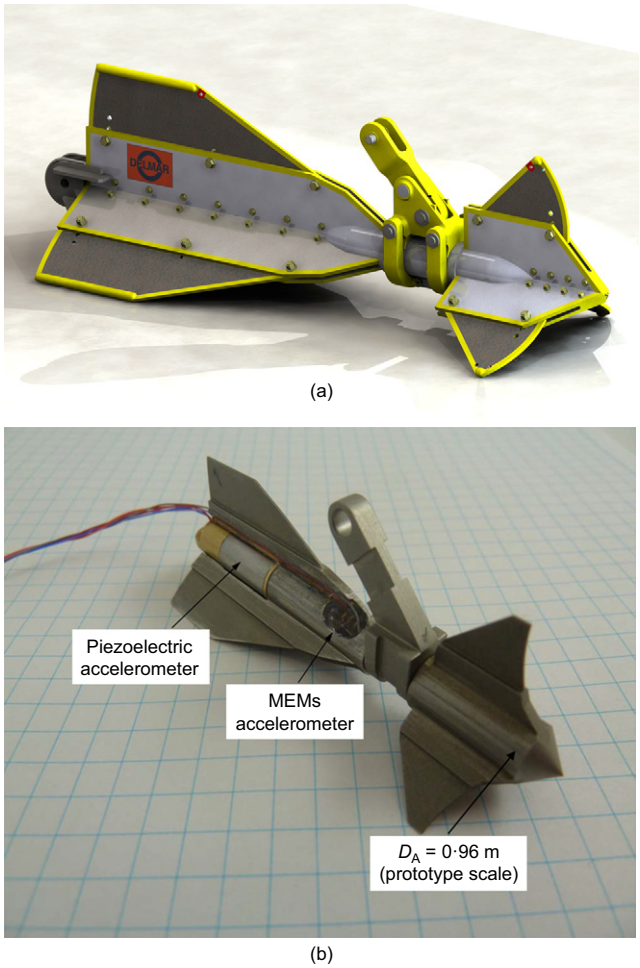

Fig. 2. (a) OMNI-Max anchor used in the field (Shelton *et al.*, 2011; anchor A1, Table 1). Copyright 2011, Society of Petroleum Engineers Inc (SPE). Reproduced with permission of SPE. Further reproduction prohibited without permission. (b) Model anchor used in centrifuge tests (O'Loughlin *et al.*, 2014; anchor A2, Table 1) (MEMS: micro-electromechanical system)

to ensure that the soil extensions were sufficiently large to avoid boundary effect in dynamic analyses. A typical mesh is shown in Fig. 3. The Eulerian mesh comprised eight-noded linear brick elements (termed EC3D8R in Abaqus) with reduced integration, and a fine mesh zone was generated to accommodate the anchor trajectory during the entire installation. A 3 m thick void (i.e. material free initially) layer was set above the soil surface (see Fig. 3(c)), allowing the soil to heave by flowing into the empty Eulerian elements during the penetration process. The anchor was simulated as a rigid body.

The installation of OMNI-Max anchors in clay is completed under undrained conditions. The soil was thus modelled as an elasto-perfectly plastic material obeying a Tresca yield criterion, but extended as described later to capture strain-rate and strain-softening effects. A user subroutine was implemented to track the evolving soil strength profile. The elastic behaviour was defined by a Poisson's ratio of 0·49 and Young's modulus of $500s_u$ throughout the soil profile. Total stress analyses were carried out adopting a uniform effective unit weight of 6 kN/m^3 over the soil depth, representing a typical average value for field conditions.

The soil–anchor interface was modelled as a frictional contact, using a general contact algorithm and specifying a (total stress) Coulomb friction law together with a limiting shear stress (τ_{max}) along the anchor–soil interface. The Coulomb friction coefficient (i.e. the ratio of shear stress to normal stress at the interface) was set to a high value of $\mu_C = 50$, in order to allow the value of τ_{max} to govern failure

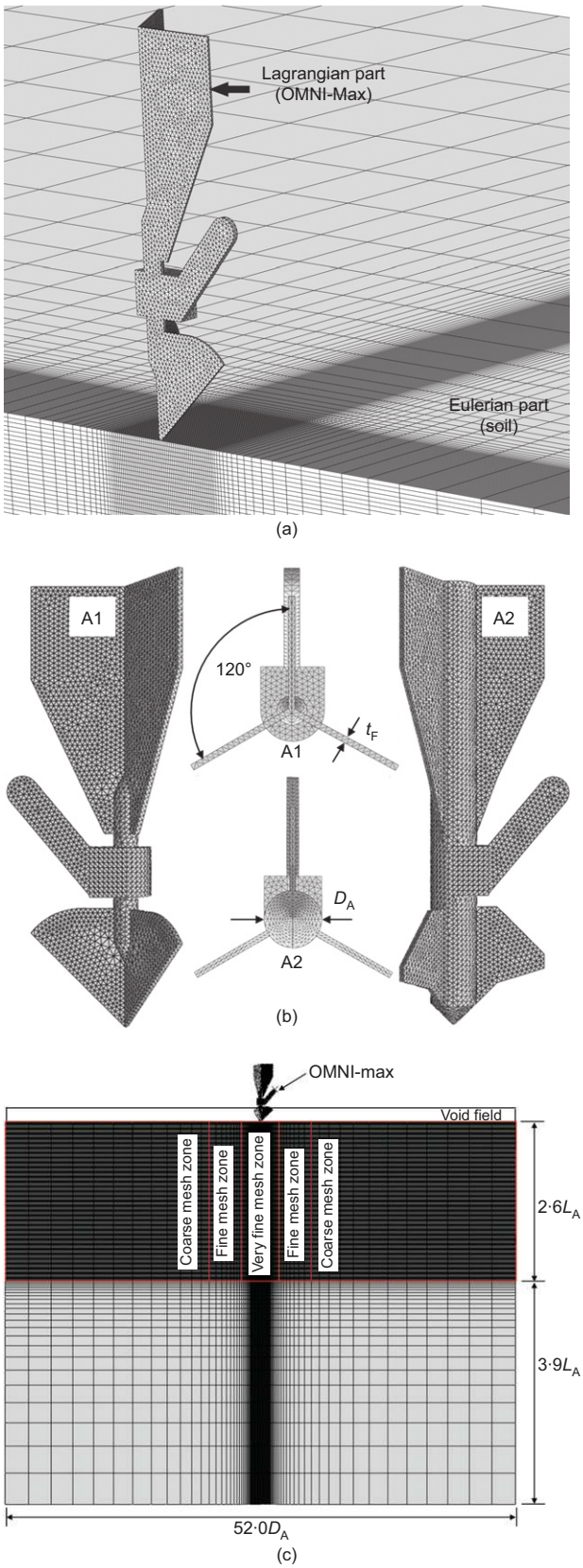

Fig. 3. Typical mesh used in CEL analysis: (a) typical 3D mesh; (b) anchor modelling; (c) side view

(Ma *et al.*, 2014). With the CEL approach, the value of the limiting interface friction must be set prior to the analysis, before the value of the 'adjacent' soil strength is known. To overcome this difficulty, for each case, the limiting interface friction was determined by: (*a*) simulating anchor penetration with frictionless contact; (*b*) obtaining the final anchor tip penetration depth and calculating $s_{u,ref}$ at that depth; and (*c*) setting τ_{max} equal to an interface friction ratio, α, times the calculated $s_{u,ref}$ at the final tip depth, with α taken as the inverse soil sensitivity, $1/S_t$ (Hossain & Randolph, 2009; Zhou & Randolph, 2009; O'Loughlin *et al.*, 2013). Owing to the limitation of the current CEL approach, τ_{max} is a constant value on all the anchor surfaces during the entire calculation. At shallow depth, where τ_{max} may exceed the rate-dependent shear strength of the adjacent soil, failure may occur in the adjacent soil, rather than at the interface. The contact interface is created between Lagrangian mesh and Eulerian material, and automatically computed and tracked during the analysis.

Incorporation of combined effects of strain rate and strain softening

The Tresca soil model was extended in order to consider the combined effects of rate dependency and gradual softening, following the models of Herschel–Bulkley (H–B; Herschel & Bulkley, 1926) and Einav–Randolph (E–R; Einav & Randolph, 2005), respectively. The undrained shear strength at individual Gauss points was modified immediately, according to the average rate of maximum shear strain in the previous time step and the current accumulated absolute plastic shear strain, according to (Zhu & Randolph, 2011; Boukpeti *et al.*, 2012; Hossain *et al.*, 2015)

$$s_u = \left[1 + \eta\left(\frac{\dot{\gamma}}{\dot{\gamma}_{ref}}\right)^{\beta}\right]\left[\delta_{rem} + (1 - \delta_{rem})e^{-3\xi/\xi_{95}}\right]\frac{s_{u,ref}}{(1+\eta)} \quad (1)$$

where $s_{u,ref}$ is the shear strength at the reference shear strain rate of $\dot{\gamma}_{ref}$. The first bracketed term of equation (1) augments the strength according to the operative shear strain rate, $\dot{\gamma}$, relative to a reference value, $\dot{\gamma}_{ref}$, which is typically around 10^{-5} s^{-1} for laboratory element tests and up to $\sim 0{\cdot}5$ s^{-1} for field penetrometer testing (although in the latter case the high strain rate is partly compensated for by strain softening (Zhou & Randolph, 2009)). Ideally, the shear strength should be deduced from a reference strain rate, $\dot{\gamma}_{ref}$, that is relatively close (within 2–3 orders of magnitude) to that relevant for the application. The parameter η is a viscous property and β the shear-thinning index (or rate parameter). Boukpeti *et al.* (2012) carried out a series of undrained shear strength measurements on two different clays from fall-cone tests, vane shear, T-bar and ball penetrometer tests. They reported typical values of η and β in the ranges of 0·1–2·0 and 0·05–0·15, respectively, using $\dot{\gamma}_{ref} = 0{\cdot}06$ s^{-1}. O'Loughlin *et al.* (2013) and Chow *et al.* (2014) used $\dot{\gamma}_{ref} = 0{\cdot}17$ s^{-1} and 0·1 s^{-1} for analysing centrifuge test data from installation of torpedo anchors and a dynamic cone penetrometer, respectively, in clay. Based on these, and through back-figuring reported field data and centrifuge test data in clay with sensitivity $S_t =$ 2–5, here a value of $\dot{\gamma}_{ref} = 0{\cdot}1$ s^{-1} and rate parameters $\eta = 1{\cdot}0$ and $\beta = 0{\cdot}1$ were adopted.

The second part of equation (1) models the degradation of strength according to an exponential function of cumulative plastic shear strain, ξ, from the intact condition to a fully remoulded ratio, δ_{rem} (the inverse of the sensitivity, S_t). The relative ductility is controlled by the parameter, ξ_{95}, which represents the cumulative plastic shear strain required for 95% remoulding. Typical values of ξ_{95} have been estimated as around 10–30 (i.e. 1000–3000% shear strain; Zhou & Randolph, 2009).

RESULTS AND DISCUSSION

A systematic parametric study was carried out varying various influencing factors: (*a*) the impact velocity (v_i = 15–30 m/s); (*b*) the soil undrained shear strength ($s_{u,ref}$ = 2·4 + 1·1*z* kPa, 5 + 2*z* kPa and 10 + 3*z* kPa); and (*c*) the anchor submerged weight (W_s = 311–663 kN). The results from this parametric study, as assembled in Table 2, are discussed below starting with the validation exercise.

Validation against field data

The LDFE results were validated against field data reported by Zimmerman *et al*. (2009) and Shelton *et al*. (2011), as noted in the second section of this paper ('Reported data from field installation'). Eight embedment depths were selected, as listed by Zimmerman *et al*. (2009). An LDFE analysis was carried out using v_i = 19 m/s and $s_{u,ref}$ = 2·4 + 1·1*z* kPa (η = 1·0; β = 0·1; $\dot{\gamma}_{ref}$ = 0·1 s^{-1}; δ_{rem} = 1/S_t = 1/3; ξ_{95} = 20). Fig. 4 shows the computed time–tip penetration profile and measured final embedment depths. The results are consistent, confirming the capability and accuracy of the numerical model in assessing the embedment depth during dynamic installation of OMNI-Max anchors in clay soil.

Embedment depth $d_{e,t}$

In order to demonstrate the effect of various factors, the tip embedment depths, $d_{e,t}$, are presented as a function of impact velocity, v_i, in Fig. 5 and Table 2. The numerical results indicate that the embedment depth increases (linearly) with the impact velocity and anchor weight. The reverse trend is evident with increasing soil strength. Three interesting features are discussed below.

(*a*) Soil failure mechanisms: Fig. 6 depicts the instantaneous (resultant) velocity vectors during penetration of the A1 OMNI-Max anchor in clay with different undrained shear strength profiles (note, the instantaneous velocity vector plots are not the same as for the real Lagrangian material, but the representation of the deformed soil flow in Eulerian element; e.g. Tho *et al*. (2013)). Because of autoscaling, the regions of vectors extend out to a velocity of approximately 0·5% of the current anchor velocity. This shows the soil failure mechanisms at four different times after impacting the soil surface: (i) immediately after impacting the seafloor; (ii) significant soil movement occurring adjacent to the embedded anchor; (iii) the soil incremental displacement that is concentrated at head fins and padeye; and (iv) finally, the velocities in the soil decreasing towards zero as the anchor reaches its final embedment depth, coming to rest. The deceleration of the anchor in clay with higher soil strength ($s_{u,ref}$ = 10 + 3*z* kPa) is much greater than that in softer clay ($s_{u,ref}$ = 2·4 + 1·1*z* kPa) resulting in a lower embedment depth (see Fig. 6).

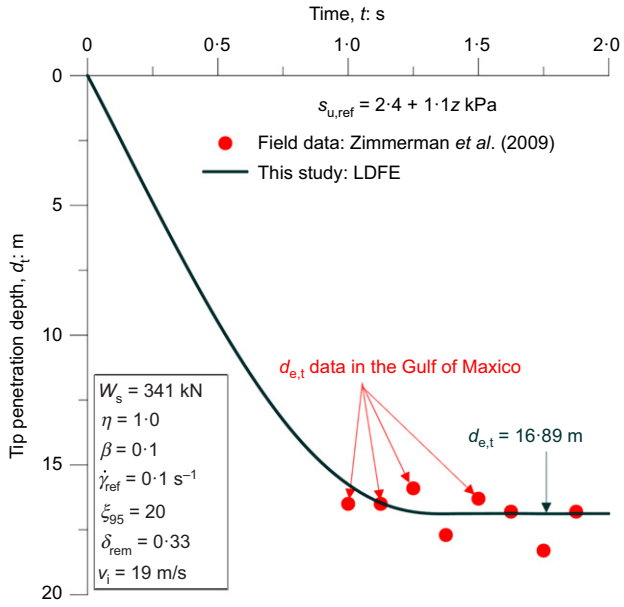

Fig. 4. Comparison between LDFE result and measured field installation data (anchor A1)

Table 2. Summary of 3D LDFE analyses performed

Group (Anchor type)	Submerged anchor weight, W_s: kN	v_i: m/s	$s_{u,ref}$: kPa	Depth of tip embedment, $d_{e,t}$: m	Notes
I (A1)	341	15	2·4 + 1·1*z*	15·1	Effect of impact velocity
		19		16·89	
		25		19·59	
		30		21·82	
II (A1)	341	15	5 + 2*z*	11·24	Effect of soil strength
		20		13·16	
		25		15·10	
		30		17·75	
III (A1)	341	15	10 + 3*z*	8·69	
		20		10·37	
		25		12·05	
		30		13·69	
IV (A1)	311	19	2·4 + 1·1*z*	15·89	Effect of anchor weight
		30		20·60	
	341	19		16·89	
		30		21·82	
	371	19		17·83	
		30		23·02	
V (A2)	555	19	2·4 + 1·1*z*	22·63	Effect of anchor geometry
	609			24·15	
	663			25·70	

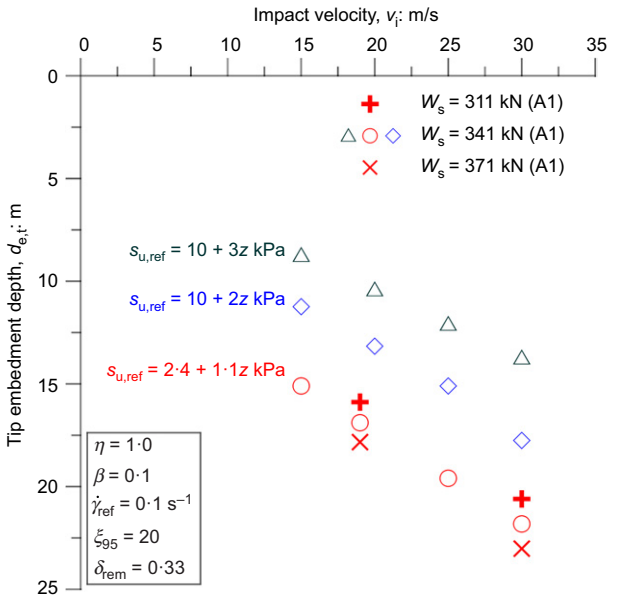

Fig. 5. Effect of various factors on anchor tip embedment depth (anchor A1; groups I–IV, Table 2)

(*b*) Effect of anchor weight: Fig. 7 shows the effect of anchor submerged weight and geometry plotting the anchor penetration depth, as a function of time and velocity of the anchor, in soft clay with $s_{u,ref} = 2{\cdot}4 + 1{\cdot}1z$ kPa (in groups IV and V, Table 2). The results indicate that the anchor penetration profile can be divided into two stages. Stage 1 corresponds to shallow penetration where the anchor accelerates, although it advances into the soil. The soil resistance was less than the submerged weight of the anchor. The effect of the 10–20% greater submerged anchor weight is minimal at the depth of stage 1. In stage 2, at greater penetration, the frictional and end bearing resistance, along with the inertial drag, overcome the submerged weight and the anchor decelerates. It should be noted that, if an anchor impacts the seabed with the terminal velocity, stage 1 is diminished, leading to deceleration of the anchor more or less from the mudline (see e.g. Fig. 6).

(*c*) Cavity condition during penetration: the effect of soil undrained shear strength on cavity depth is illustrated in Fig. 8. It can be seen that (i) for clay with lowest $s_{um,ref}/\gamma' D_p = 0{\cdot}26$ (Figs 8(a) and 8(d)), the anchor becomes essentially fully covered by the backfilled soil; (ii) for clay with medium $s_{um,ref}/\gamma' D_p = 0{\cdot}53$ (Figs 8(b) and 8(d)), the soil partly flows back between tail fins and padeye, but the cavity remains somewhat open (with distorted wall); and (iii) for clay with the highest $s_{um,ref}/\gamma' D_p = 1{\cdot}06$ (Figs 8(c) and 8(d)), the cavity formed above the penetrating anchor remains open. From centrifuge model tests in clay, Hossain *et al.* (2014) also observed a fully replenished cavity for $s_{um,ref}/\gamma' D_p = 0{\cdot}12$.

PREDICTION OF EMBEDMENT DEPTH IN FIELD

Shear resistance method

The motion response of an OMNI-Max anchor during dynamic embedment in soil may be approached by considering Newton's second law of motion and the forces acting on the anchor during penetration. Several studies (e.g. True, 1974; Brandão *et al.*, 2006; Richardson *et al.*, 2009; O'Loughlin *et al.*, 2013, Chow *et al.*, 2014; Hossain *et al.*, 2014) have adopted such an approach, with variations on the inclusion and formulation of the various forces acting on the anchor. A similar approach is adopted here

$$\begin{aligned} m\frac{\mathrm{d}^2 z}{\mathrm{d}t^2} &= W_s - F_\gamma - R_{f1}F_b - R_{f2}F_f - F_d \\ &= W_s - F_\gamma - R_{f1}\left(F_{b,HF} + F_{b,PE}\right) \\ &\quad - R_{f2}\left(F_{f,HF} + F_{f,PE} + F_{f,TF}\right) - F_d \\ &= W_s - F_\gamma - R_{f1}\left(N_{c,bF}\, s_{u,tHF}\, A_{bHF} + N_{c,bP}\, s_{u,bPE}\, A_{bPE}\right) \\ &\quad - \alpha R_{f2}\left(s_{u,sHF}\, A_{sHF} + s_{u,sPE}\, A_{sPE} + s_{u,sTF}\, A_{sTF}\right) \\ &\quad - \frac{1}{2} C_d\, \rho_s\, A_p\, v^2 \end{aligned} \tag{2}$$

The terms used in the above expression are defined under the notation list. R_{f1} and R_{f2} reflect the effects of shear strain rate for end bearing and frictional resistance, respectively. The frictional resistance term (F_f) comprises friction along the head fins ($F_{f,HF}$) and the tail fins ($F_{f,TF}$), while the bearing resistance term (F_b) includes end bearing at the top of the head fins ($F_{b,HF}$) and base of the padeye ($F_{b,PE}$). W_s is the submerged weight (in water) of the anchor and F_γ is a buoyancy force, calculated as the displaced volume times the

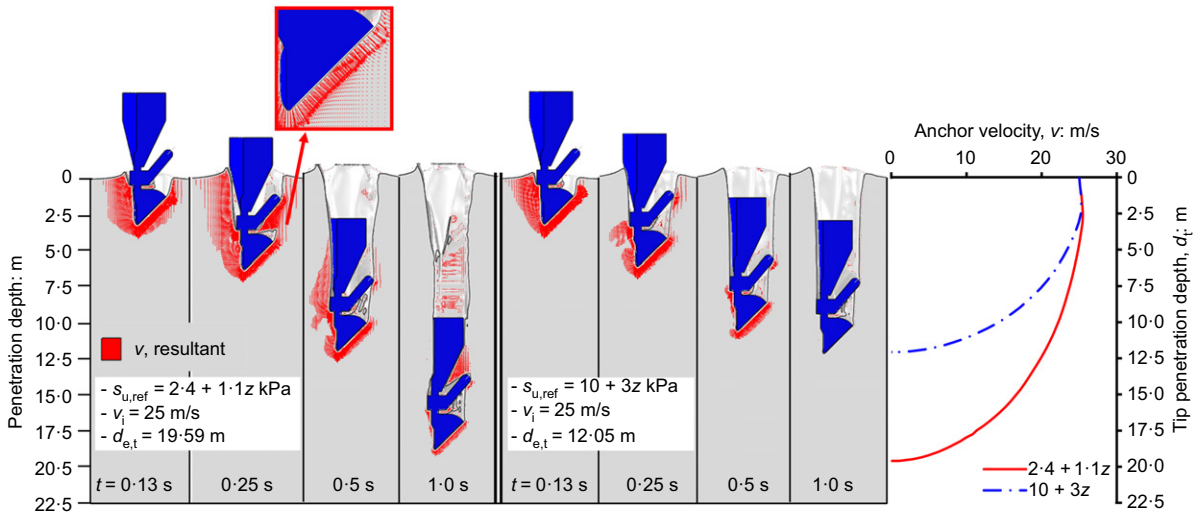

Fig. 6. Instantaneous (resultant) velocity vectors with anchor embedment (anchor A1; in groups I and III, Table 2)

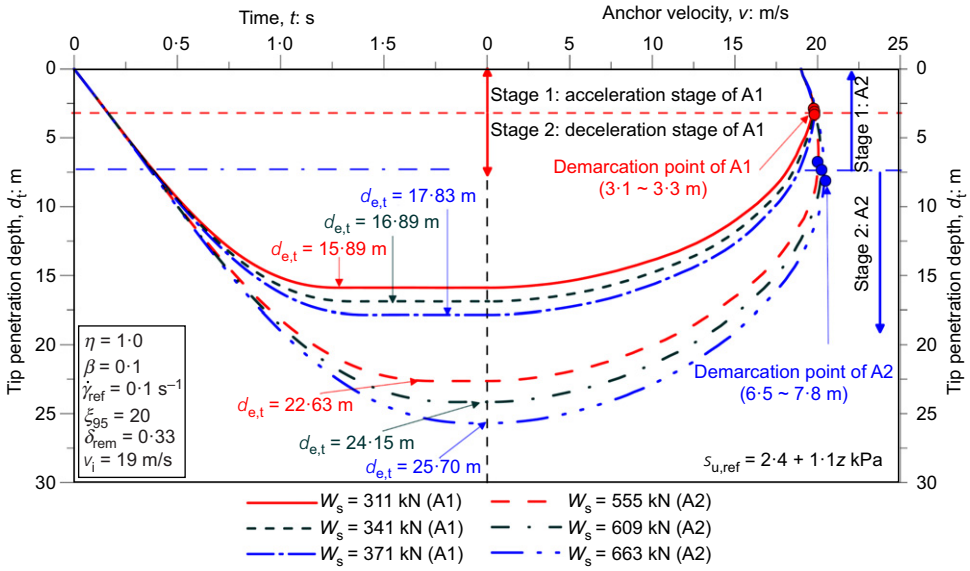

Fig. 7. Effect of anchor submerged weight and geometry on penetration profile (anchors A1 and A2; in groups IV and V, Table 2)

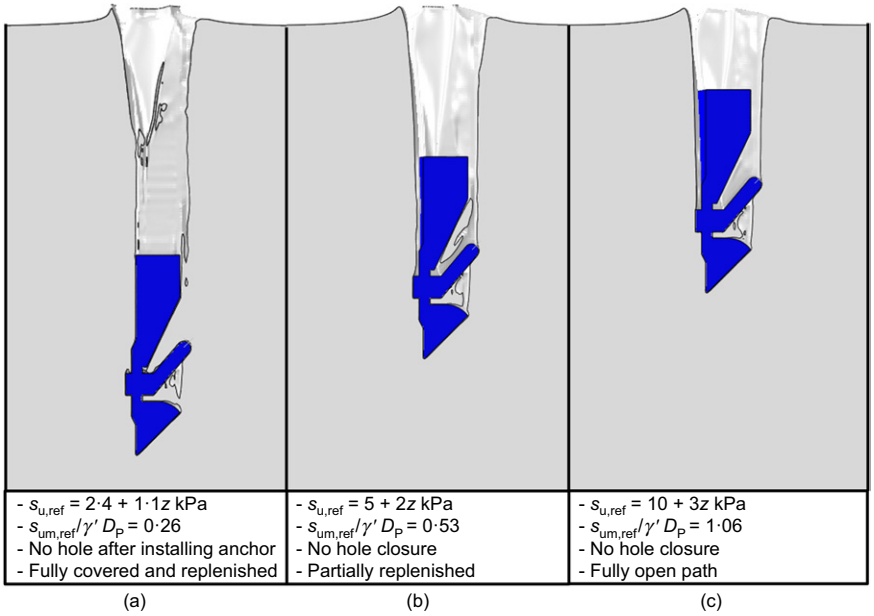

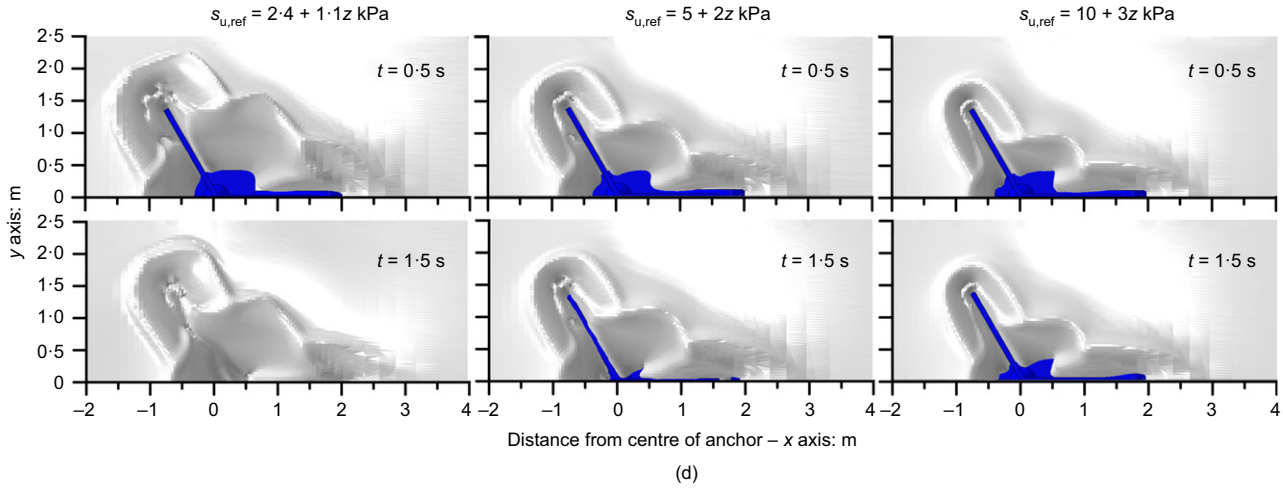

Fig. 8. Effect of soil strength on cavity condition above installed anchor (anchor A1): (a) $s_{u,ref} = 2{\cdot}4 + 1{\cdot}1z$ kPa; (b) $s_{u,ref} = 5 + 2z$ kPa; (c) $s_{u,ref} = 10 + 3z$ kPa; (d) plan view of cavity condition

effective unit weight of the soil (γ'). Note, $(W_s - F_\gamma)$ represents the submerged weight of the anchor in soil, W_{ss}. F_d is the inertial 'drag' resistance generally expressed in terms of a drag coefficient, C_d, as indicated (with ρ_s the soil submerged density and v the penetration velocity). Owing to geometrical similarity, deep bearing factors of cone and strip footing of 13·6 (Low *et al.*, 2010) and 7·5 (Skempton, 1951) were adopted for $N_{c,bP}$ and $N_{c,bF}$, respectively. The R_{f1} term was calculated using the rate-dependent term of equation (1) as

$$R_{f1} = \left[1 + \eta\left(\frac{nv/D_p}{\dot{\gamma}_{ref}}\right)^{\beta}\right]\frac{1}{(1+\eta)} \quad (3)$$

In this study, values for the various parameters were adopted as follows: $C_d = 0{\cdot}63$, $n = 1{\cdot}0$, $N_{c,bP} = 13{\cdot}56$, $N_{c,bF} = 7{\cdot}5$, $\eta = 1{\cdot}0$, $\beta = 0{\cdot}1$, $\dot{\gamma}_{ref} = 0{\cdot}1\ s^{-1}$ and $\alpha = 1/S_t = 0{\cdot}33$. For the frictional resistance, R_{f2} was taken as $2R_{f1}$ from previous reports (Einav & Randolph, 2006; Chow *et al.*, 2014; Steiner *et al.*, 2014).

Figure 9 shows the computed (LDFE analysis) and predicted velocity–penetration profiles using equations (2) and (3) ($s_{u,ref} = 5 + 2z$). The estimated profiles assuming ideal rate-independent ($\eta = 0$; equations (1) and (3)) soil are also included in the figure for comparison. Overall, the curves using equations (2) and (3) closely predict the general trend of the LDFE results (for $S_t = 3{\cdot}0$), including the embedment depths ($d_{e,t}$) with an error of $< \pm 3{\cdot}0\%$. Significantly higher embedment depths were resulted for ideal soil, confirming the necessity of considering, in particular, rate dependency of the undrained shear strength for this dynamic installation problem.

Modified energy method

O'Loughlin *et al.* (2013) proposed a simple expression for conservatively estimating the embedment of DIAs in clay. Total energy, defined as the sum of the kinetic and potential energy (relative to the final embedment depth) of the anchor at the mudline, and soil strength gradient (k) were expressed in terms of normalised embedment depth as

$$\frac{d_{e,t}}{D_p} \approx \left(\frac{E_{total}}{kD_p^4}\right)^{p} \quad (4)$$

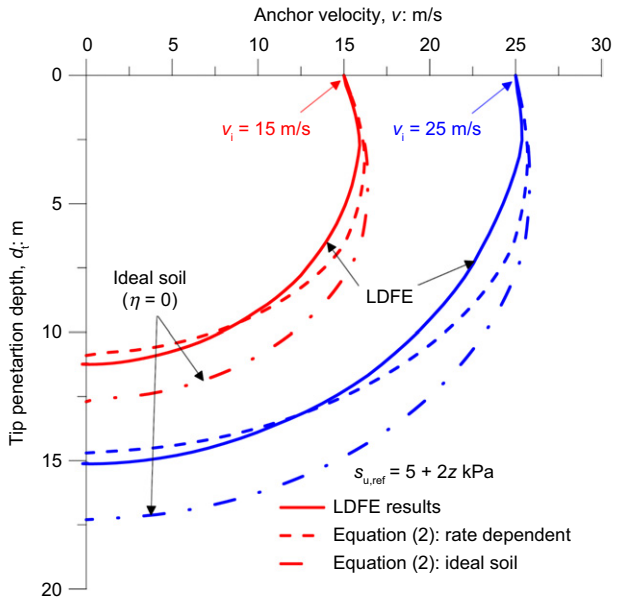

Fig. 9. Prediction for anchor embedment depth in clay using shear resistance method (anchor A1)

where

$$E_{total} = \frac{1}{2}mv_i^2 + m'gd_{e,t} \quad (5)$$

In equation (5), a somewhat equivalent effective mass, m', is used in the second term (left-hand side) because '$m'g$' (where g is Earth's gravitational acceleration = 9·81 m/s^2) represents the submerged weight of the anchor in soil. Fig. 10(a) compares field data for clay reported by Zimmerman *et al.* (2009) with LDFE data from this study, showing excellent agreement. The best fit between the OMNI-Max data (from the field and LDFE) and equation (4) is obtained using $p = 0{\cdot}32$ (standard deviation of $(d_{e,t})_{predicted}/(d_{e,t})_{measured + LDFE}$ of 0·056), compared with $p = 0{\cdot}33$ as originally proposed by O'Loughlin *et al.* (2013).

An alternative version of this expression, accounting for anchor total surface area ($A_s = A_{sHF} + A_{sPE} + A_{sTF}$) and an effective soil strength gradient ($k_{eff} = (s_{um,ref} + kd_{e,t})/d_{e,t}$), was

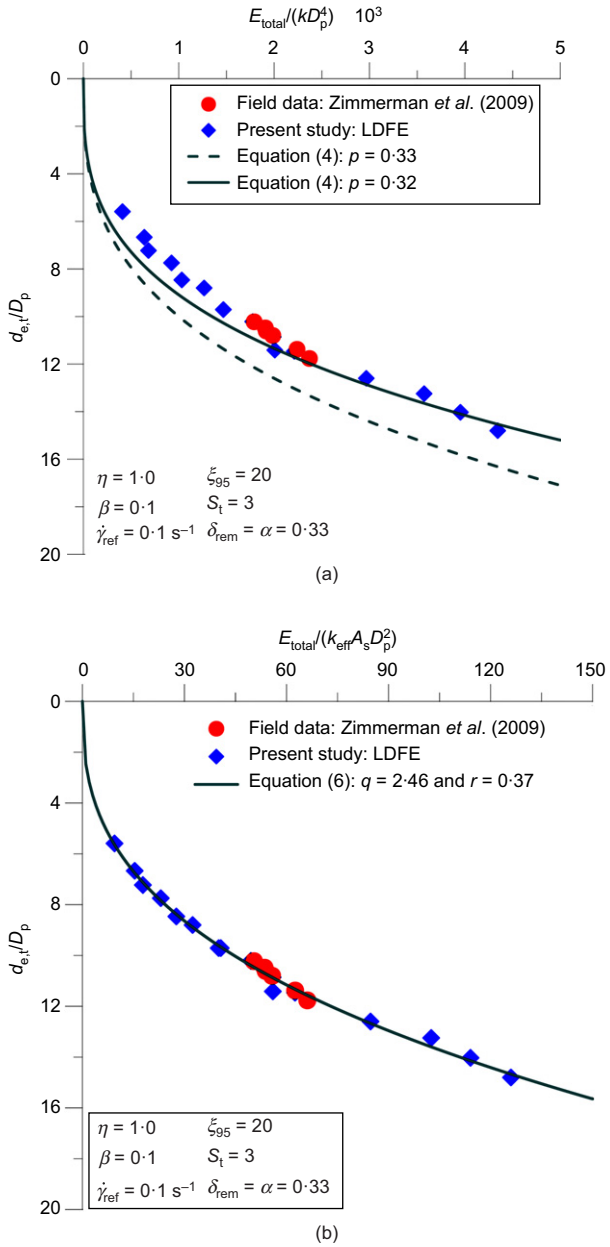

Fig. 10. New methods for assessing anchor embedment depths (anchors A1 and A2; groups I–V, Table 2): (a) total energy method; (b) modified total energy method

proposed as

$$\frac{d_{e,t}}{D_p} \approx q\left(\frac{E_{total}}{k_{eff} A_s D_p^2}\right)^r \quad (6)$$

where $q = 2{\cdot}46$ and $r = 0{\cdot}37$ provide an excellent fit to the field and LDFE results, as demonstrated by Fig. 10(b), with standard deviation of $(d_{e,t})_{predicted}/(d_{e,t})_{measured+LDFE}$ of 0·015.

CONCLUDING REMARKS

Dynamic installation of OMNI-Max anchors was investigated extensively through 3D dynamic LDFE analyses. Insight into the behaviour of OMNI-Max anchors during dynamic installation in non-homogeneous clay was illustrated through plotting instantaneous (resultant) velocity vectors, the anchor full penetration process and cavity condition above the installing anchor. The effects of various factors related to impact velocity, anchor geometric dimensions and submerged weight, and soil strength were highlighted.

For assessing the dynamic embedment depth of OMNI-Max anchors two models were proposed: (*a*) a shear resistance method including rate-dependent undrained shear strength of clay (with suggested values of the rate parameters); (*b*) total energy based expressions taking into account the effect of anchor mass, impact velocity, surface area, projected area equivalent diameter of the anchor and the gradient of the soil undrained shear strength. The LDFE results and field data were used to calibrate the models, with excellent agreement shown not only in terms of the final embedment depth (with an error of $< \pm 3{\cdot}0\%$) but also the full penetration profile.

ACKNOWLEDGEMENTS

The research presented here was undertaken with support from the Australian Research Council (ARC) through the Discover Early Career Researcher Award DE140100903. The work forms part of the activities of the Centre for Offshore Foundation Systems (COFS), currently supported as a node of the Australian Research Council Centre of Excellence for Geotechnical Science and Engineering, through Centre of Excellence funding from the State Government of Western Australia and in partnership with The Lloyd's Register Foundation. This support is gratefully acknowledged.

NOTATION

A_{bHF} head fins projected area
A_{bPE} padeye projected area
A_p anchor frontal projected area
A_s embedded anchor total surface area
A_{sHF} embedded head fins shaft surface area
A_{sPE} embedded padeye surface area
A_{sTF} embedded tail fins surface area
C_d drag coefficient
D_A anchor shaft diameter
D_p anchor frontal projected area equivalent diameter (including fins and padeye)
$d_{e,t}$ anchor tip embedment (final penetration) depth
d_t anchor tip penetration depth
E_{total} total energy during anchor penetration
F_b end bearing resistance
$F_{b,HF}$ end bearing resistance at base of head fins
$F_{b,PE}$ end bearing resistance at base of padeye
F_d inertial drag resistance
F_f frictional resistance
$F_{f,HF}$ frictional resistance along head fins
$F_{f,PE}$ frictional resistance along padeye
$F_{f,TF}$ frictional resistance along tail fins
F_γ buoyant weight of soil displaced by anchor
$\boldsymbol{g}$ Earth's gravitational acceleration
H_P padeye height
h_d anchor drop height
k shear strength gradient with depth
k_{eff} effective soil strength gradient
L_A anchor shaft length
L_{HF} head fin length
L_{PE} padeye length
L_{TF} tail fin length
m dry mass of anchor
m' effective mass of anchor (submerged in soil)
$N_{c,bF}$ bearing capacity factor at base of anchor fins
$N_{c,bP}$ bearing capacity factor at base of padeye body
n factor relating operative shear strain rate to normalised velocity
p, r, q exponents and coefficient of energy models
R_{f1} factor related to effect of strain rate for end bearing resistance
R_{f2} factor related to effect of strain rate for frictional resistance
S_t soil sensitivity
s_u undrained shear strength
s_{um} undrained shear strength at mudline
$s_{um,ref}$ reference undisturbed soil strength at mudline
$s_{u,tHF}$ undrained shear strength at top of head fins
$s_{u,bPE}$ undrained shear strength at bottom of padeye
$s_{u,sHF}$ average undrained shear strength over embedded length of head fins
$s_{u,sPE}$ average undrained shear strength over embedded length of padeye
$s_{u,sTF}$ average undrained shear strength over embedded length of tail fins
$s_{u,ref}$ reference undrained shear strength
t time after anchor tip impacting seabed
t_F fin thickness
V_A anchor volume
v anchor penetrating velocity
v_i anchor impact velocity
W_d anchor dry weight
W_s anchor submerged weight in water
W_{ss} anchor submerged weight in soil
w_F fin width
w_P padeye lever arm
z depth below soil surface
α interface friction ratio
β shear-thinning index (rate parameter in the Herschel–Bulkley model)
γ' effective unit weight of soil
$\dot{\gamma}$ shear strain rate
$\dot{\gamma}_{ref}$ reference shear strain rate
δ_{rem} remoulded strength ratio
η viscous property
μ_c Coulomb friction coefficient
ξ cumulative plastic shear strain
ξ_{95} cumulative plastic shear strain required for 95% remoulding
ρ_s submerged density of soil
τ_{max} limiting shear strength at soil–anchor interface

REFERENCES

Boukpeti, N., White, D. J. & Randolph, M. F. (2012). Strength of fine-grained soils at the solid–fluid transition. *Géotechnique* **62**, No. 3, 213–226, http://dx.doi.org/10.1680/geot.9.P.069.

Brandão, F. E. N., Henriques, C. C. D., de Araujo, J. B., Ferreira, O. C. G. & dos Santos Amaral, C. (2006). Albacora Leste field development – FPSO P-50 mooring system concept and installation. *Proceedings of the offshore technology conference*, Houston, TX, paper OTC18243.

Chow, S. H., O'Loughlin, C. D. & Randolph, M. F. (2014). Soil strength estimation and pore pressure dissipation for free-fall piezocone in soft clay. *Géotechnique* **64**, No. 10, 817–824, http://dx.doi.org/10.1680/geot.14.P.107.

de Araujo, J. B., Machado, R. D. & de Medeiros Junior, C. J. (2004). High holding power torpedo pile – results for the first long

term application. *Proceedings of international conference on ocean, offshore and arctic engineering*, Vancouver, Canada, OMAE2004-51201.

Dassault Systèmes (2011). *Abaqus, Version 6.11 EF documentation*. Providence, RI, USA: Hibbitt, Karlsson and Sorensen, Inc.

Einav, I. & Randolph, M. F. (2005). Combining upper bound and strain path methods for evaluating penetration resistance. *Int. J. Numer. Methods Engng* **63**, No. 14, 1991–2016.

Einav, I. & Randolph, M. F. (2006). Effect of strain rate on mobilised strength and thickness of curved shear bands. *Géotechnique* **56**, No. 7, 501–504, http://dx.doi.org/10.1680/geot.2006.56.7.501.

Herschel, W. H. & Bulkley, T. (1926). Measurement of consistency as applied to rubber-benzene solutions. *Proc. Am. Soc. Testing Mater.* **26**, No. 2, 621–633.

Hossain, M. S. & Randolph, M. F. (2009). Effect of strain rate and strain softening on the penetration resistance of spudcan foundations on clay. *Int. J. Geomech., ASCE* **9**, No. 3, 122–132.

Hossain, M. S., Kim, Y. H. & Gaudin, C. (2014). Experimental investigation of installation and pull-out of dynamically penetrating anchors in clay and silt. *J. Geotech. Geoenviron. Engng, ASCE* **140**, No. 7, 04014026.

Hossain, M. S., O'Loughlin, C. & Kim, Y. H. (2015). Dynamic installation and monotonic pullout of a torpedo anchor in calcareous silt. *Géotechnique* **65**, No. 2, 77–90, http://dx.doi.org/10.1680/geot.13.P.153.

Kim, Y. H., Hossain, M. S. & Wang, D. (2014). Numerical modelling of dynamic installation of a torpedo anchor in calcareous silt. *Proceedings of the international offshore and polar engineering conference*, ISOPE, Busan, Korea, pp. 687–692.

Kim, Y. H., Hossain, M. S. & Wang, D. (2015). Effect of strain rate and strain softening on embedment depth of a torpedo anchor in clay. *Ocean Engng*, in press.

Lieng, J. T., Tjelta, T. I. & Skaugset, K. (2010). Installation of two prototype deep penetrating anchors at the Gjoa Field in the North Sea. *Proceedings of the offshore technology conference*, Houston, TX, paper OTC20758.

Low, H. E., Lunne, T., Andersen, K. H., Sjursen, M. A., Li, X. & Randolph, M. F. (2010). Estimation of intact and remoulded undrained shear strengths from penetration tests in soft clays. *Géotechnique* **60**, No. 11, 843–859, http://dx.doi.org/10.1680/geot.9.P.017.

Ma, J., Wang, D. & Randolph, M. F. (2014). A new contact algorithm in the material point method for geotechnical simulations. *Int. J. Numer. Analyt. Methods Geomech.* **38**, No. 11, 1197–1210.

Medeiros, C. J. Jr (2002). Low cost anchor system for flexible risers in deep waters. *Proceedings of the offshore technology conference*, Houston, TX, paper OTC14151.

Nazem, M., Carter, J. P., Airey, D. W. & Chow, S. H. (2012). Dynamic analysis of a smooth penetrometer free-falling into uniform clay. *Géotechnique* **62**, No. 10, 893–905, http://dx.doi.org/10.1680/geot.10.P.055.

Nie, C. & Shelton, J. (2011). Prediction of gravity installed anchors installation penetration. *Proceedings of oceans '11 MTS/IEEE KONA*, IEEE, Hawaii, USA, pp. 1845–1849.

O'Loughlin, C. D., Randolph, M. F. & Richardson, M. D. (2004). Experimental and theoretical studies of deep penetrating anchors. *Proceedings of the offshore technology conference*, Houston, TX, paper OTC16841.

O'Loughlin, C. D., Richardson, M. D., Randolph, M. F. & Gaudin, C. (2013). Penetration of dynamically installed anchors in clay. *Géotechnique* **63**, No. 11, 909–919, http://dx.doi.org/10.1680/geot.11.P.137.

O'Loughlin, C. D., Morton, J. P., Gaudin, C. & White, D. J. (2014). MEMS accelerometers for measuring dynamic penetration events in geotechnical centrifuge tests. *Int. J. Phys. Modelling Geotech.* **14**, No. 2, 31–39.

Richardson, M. D., O'Loughlin, C. D., Randolph, M. F. & Gaudin, C. (2009). Setup following installation of dynamic anchors in normally consolidated clay. *J. Geotech. Geoenviron. Engng, ASCE* **135**, No. 4, 487–496.

Shelton, J. T., Nie, C. & Shuler, D. (2011). Installation penetration of gravity installed plate anchors – laboratory study results and field history data. *Proceedings of the offshore technology conference*, Houston, TX, paper OTC22502.

Skempton, A. W. (1951). The bearing capacity of clays. *Proceedings of the building research congress*, London, UK, vol. 1, pp. 180–189.

Steiner, A, Kopf, A. J., L'Heureux, J. S., Kreiter, S., Stegmann, S., Haflidason, H. & Moerz, T. (2014). In situ dynamic piezocone penetrometer tests in natural clayey soils – a reappraisal of strain-rate corrections. *Can. Geotech. J.* **51**, No. 3, 272–288.

Tho, K. K., Leung, C. F., Chow, Y. K. & Swaddiwudhipong, S. (2013). Eulerian finite-element simulation of spudcan–pile interaction. *Can. Geotech. J.* **50**, No. 6, 595–608.

True, D. G. (1974). Rapid penetration into seafloor soils. *Proceedings of the offshore technology conference*, Houston, TX, paper OTC2095.

Zhou, H. & Randolph, M. F. (2009). Resistance of full-flow penetrometers in rate-dependent and strain-softening clay. *Géotechnique* **59**, No. 2, 79–86, http://dx.doi.org/10.1680/geot.2007.00164.

Zhu, H. & Randolph, M. F. (2011). Numerical analysis of a cylinder moving through rate-dependent undrained soil. *Ocean Engng* **38**, No. 7, 943–953.

Zimmerman, E. H., Smith, M. W. & Shelton, J. T. (2009). Efficient gravity installed anchor for deep water mooring. *Proceedings of the offshore technology conference*, Houston, TX, paper OTC20117.